Journal of Applied Fluid Mechanics, Vol. 12, No. 1, pp. 311-318, 2019.
Available online at www.jafmonline.net, ISSN 1735-3572, EISSN 1735-3645.
DOI: 10.29252/jafm.75.253.29193

Numerical Simulation of Tidal Bore Bono at Kampar River

A. C. Bayu[1], S. R. Pudjaprasetya[1], U. J. Wisha[2] and S. Husrin[3]

[1] *Industrial & Financial Mathematics Research Group, Faculty of Mathematics & Natural Sciences, Institut Teknologi Bandung, Jalan Ganesha 10, Bandung, 40132, Indonesia*
[2] *Research Institute For Coastal Resources and Vulnerability, Ministry of Marine Affairs and Fisheries, The Republic of Indonesia, Jalan Raya Padang-Painan KM. 16 Bungus, Padang, 25245, Indonesia*
[3] *Marine Research Center, Ministry of Marine Affairs and Fisheries, The Republic of Indonesia, Jalan Pasir Putih II Ancol Timur, Jakarta, 14430, Indoneisa*

Corresponding Author Email: srpudjap@gmail.com

(Received May 13, 2018; accepted August 3, 2018)

ABSTRACT

A tidal bore is a natural phenomenon usually occur in bays with large tidal waves. Sometimes this large tidal inflow are channeled deep into a river. In Indonesia, this natural phenomenon is found in the Kampar River, which is known as the tidal bore Bono. Sometimes, these tidal bore phenomena disappear, as happened to the Mascaret, tidal bore on the River Seine France. Through an understanding of the formation of tidal bore mechanism, there is hope that the tidal bore Bono in Kampar River can be preserved. In this paper, the occurrence of tidal bore Bono is simulated using the non-hydrostatic Saint-Venant equation under a staggered grid formulation. To test the accuracy of the implementation, several scenarios of hydraulic jumps were simulated first. The numerical results have shown to quantitatively confirm the analytical formula of bore height and velocity, two parameters that are important to characterize a bore wave. Further, by adopting a model that incorporates the non-hydrostatic pressure, our simulation shows the appearance of an undular bore accompanying the shock front. Finally, by using tidal current data measured along Kampar River estuary, our simulation that employs the actual river topography can show the appearance of tidal bore Bono. Our simulations were shown to be in fair agreement with the measurement.

Keywords: Undular bore; Saint-Venant equations; Non-hydrostatic numerical scheme.

NOMENCLATURE

A	cross section
b	river width
c	bore velocity
Fr	Froude number
g	acceleration due to gravity
h	water thickness
n	Manning friction coefficient
q	hydrodynamic pressure
S_0	surface pressure
S_f	friction slope
u	horizontal velocity
w	vertical velocity
η	free surface flow
ρ	fluid density

1. INTRODUCTION

A tidal bore is a surge wave, generated by a strong tide. During a high tide, a large amount of water rushes up estuaries and flows further up the rivers, against the river current flow. On the river, this tidal bore comes out as a surge wave of a sudden change in the water surface. In some situations, the appearance of a tidal bore is accompanied by an undulation, a train of secondary waves near the wavefront. Tidal bore on Qiantang River, China is considered as the highest, reaching a height of 9 meters (30 feet). In some other places, such as the Turnagain Arm in Alaska, the Amazon River in Brazil, and the Severn River in England, tidal bore is used for recreation. While the Mascaret is the name for a tidal bore in the Seine River, France, which is now almost gone, after the dredging of the Seine River estuary and the creation of the new canal de Tancarville completed in 1963.

In Indonesia, a tidal bore is found to emerge in Kampar River, Riau. In this tidal wave, there are seven types of undulations, they are known as the seven ghost of Bono. Over the past few years, tidal bore Bono has become a tourist destination that

attracts tourists, many of them are from abroad, who come to surf in the river. It is clear that the existence of tidal bore Bono increases the regional income, as well as Indonesian tourism in general. Therefore, we should maintain the existence of this tidal bore; natural resources in the upstream or downstream parts of the river should not be exploited, to prevent the destruction of tidal bore Bono. Finally, the existence of tidal bore Bono needs to be maintained, especially because Bono is the only tidal bore phenomenon found in Indonesia.

In this research, we examine the effect of Kampar River topography in the occurrence of tidal bore Bono. Also, we study the effect of tidal waves that collided with the river current resulting in the formation of this undular jump. Knowledge of the tide, river topography, as well as the river flow, would be very helpful to estimate the strength and size of this tidal bore, as well as to maintain its presence. Here, we study factors that influence the occurrence of a tidal bore. Through numerical simulations of the Saint-Venant equations formulated for rivers with non-constant cross-sections, we will study the effect of tidal currents (amplitude and period), and the magnitude of river flow to the size and strength of the tidal bore.

In this article, we apply the momentum conservative scheme for the Saint-Venant equation originally proposed by Stelling and Duijnmeijer (2003). This scheme is known to be a good method for simulating rapidly varied flow with a wide range of Froude number. The scheme can accurately compute the bore front location, which is an important property should be fulfilled by a numerical model for tidal bore Bono simulation. Further, an undulation that accompanies the tidal bore should be computed using a non-hydrostatic scheme. Therefore, the organization of this paper is arranged as follows. In Section 2. we discussed the mathematical model and its discrete formulation based on the momentum conservative staggered grid scheme. In Section 3., validation of the numerical scheme was conducted for various bore scenarios. In Section 4., the same set up is used, but now the non-hydrostatic scheme was adopted, an appearance of an undular bore was then simulated. Further, the numerical scheme is implemented using the Kampar River topography. Our simulation has shown that the tidal current data from the sea induced the appearance of an undular bore, shown to be in fair agreement with the measurement. Finally, in Section 5. we draw some conclusions.

2. THE MATHEMATICAL MODEL AND ITS DISCRETE FORMULATION

In general, rivers have a non-homogeneous cross section. So that simulation of river surface flow would require a heavy 3-dimensional calculation that needs large computer memory. Since river flow is a nearly one-dimensional problem, a good alternative is to apply a 1-dimensional approach in which the spatial axis is chosen along the river. As noted in Aldrighetti (2007) the proposed river flow model is the Saint-Venant equation applicable to inclined canals with arbitrary cross-sections. Later, the non-homogeneity on the vertical axis is accommodated by adopting the hydrodynamic pressure term in the model.

Consider an inclined canal with cross section A, as illustrated in Fig. 1. The fluid flow dynamics in the channel are governed by the following Saint-Venant equations

$$A_t + (Au)_x = 0, \tag{1a}$$

$$(Au)_t + (Auu)_x + gA\eta_x - gA(S_0 - S_f) = 0. \tag{1b}$$

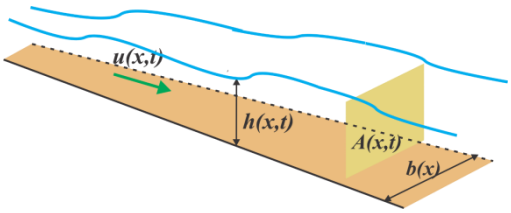

Fig. 1. A sketch of a non-homogeneous canal and variable notations.

In the above equations, $u(x,t)$ denotes the horizontal velocity of fluid particle. The cross section is $A(x,t) = b(x) \cdot h(x,t)$, where $b(x)$ is the river width, and $h(x,t)$ the water thickness. An equivalent form of the Saint Venant equations are as follows

$$(bh)_t + (bhu)_x = 0, \tag{2a}$$

$$(bhu)_t + (bhuu)_x + gbh\eta_x + gbhd_x + gbhS_f = 0. \tag{2b}$$

From Eq.$(2a)$ we obtained a relation $(bh)_t = -(bhu)_x$ and after taking $b_t = 0$, $(2b)$ is simplified to yield

$$h_t + \frac{hu}{b}b_x + (hu)_x = 0, \tag{3a}$$

$$u_t + uu_x + gh_x + \frac{gnu|u|}{h^{\frac{4}{3}}} = 0. \tag{3b}$$

Moreover, in the above equation the friction slope is approximated using the Manning formula (Vo Thi, 2008) $S_f = \frac{nu|u|}{h^{\frac{4}{3}}}$, with n is the Manning friction coefficient and for computations here we take n=0.001.

Kim and Lynett (2011) revealed that undular tidal bore phenomena need a model that incorporates a non-hydrostatic term. Here, we start from the following 2D Euler equations

$$u_t + uu_x + wu_z + gh_x + \frac{q_x}{\rho} + \frac{gnu|u|}{h^{\frac{4}{3}}} = 0, \tag{4a}$$

$$w_t + uw_x + ww_z + \frac{q_z}{\rho} = 0, \tag{4b}$$

$$u_x + w_z = 0. \tag{4c}$$

In the above formula $q(z,x,t)$ the hydrodynamic pressure, the fluid density, whereas $w(z,x,t)$ denotes the vertical velocities of fluid particles. For examining the free surface flow $\eta(x,t)$, an extra equation is obtained from the continuity equation which is integrated over the fluid depth

$$\int_{fluid\ dept} (u_x + w_z)dz = 0.$$

By incorporating the kinematic boundary conditions at the surface and along the bottom, we obtain

$$h_t + \frac{hu}{b}b_x + (hu)_x = 0, \tag{5}$$

which is indeed the mass conservation equation in $(3a)$.

Under the assumption that surface flow is horizontally dominant, the nonlinear terms wu_x, uw_x, ww_z in $(4a)$ and $(4b)$ are of high order, therefore in further discussions they are neglected. The resulting model is then

$$h_t + \frac{hu}{b}b_x + (hu)_x = 0, \tag{6a}$$

$$u_t + uu_x + gh_x + \frac{gnu|u|}{h^{\frac{4}{3}}} = 0, \tag{6b}$$

$$w_t + \frac{q_z}{\rho} = 0, \tag{6c}$$

$$u_x + w_z = 0. \tag{6d}$$

We resume here that the non-hydrostatic model is $(6a-6d)$, whereas the hydrostatic model can be directly obtained by taking $q = 0$, therefore the governing equation is just $(6a,\ 6b)$. This is in fact the Saint-Venant equation $(1a,\ 1b)$ for a rectangular channel with arbitrary width $b(x)$.

Next, we describe the non-hydrostatic staggered scheme for solving $(6a,\ 6d)$. Here, we adopt the scheme developed by Bayu *et. al.* (2017). In a computational domain $\Omega = \{(z,x)|\ -d \le z \le \eta, 0 \le x \le L\}$, the horizontal interval $[0,\ L]$ is divided into sub interval with length $\Delta x/2$, with $\Delta x = L/Nx$ to yield a staggered grid $0 = x_{\frac{1}{2}}, x_1, ..., x_j, x_{j+\frac{1}{2}}, ..., x_{N_x+\frac{1}{2}} = L$, with full grids $x_j, j = 1,2,...,N_x$ and half grids $x_{j+\frac{1}{2}}, j = 0,1,...,N_x$.

On that staggered grid, variable u is calculated at the half grids, while variables w, h and q are calculated at the full grids. Staggered grid is illustrated in Fig. 2.

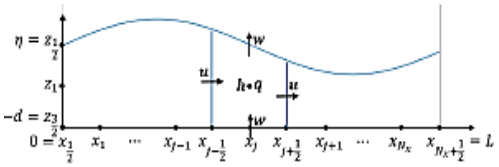

Fig. 2. A staggered grid and arrangement of unknowns in a column of mass.

Figure 2 depicts a mass cell centered at (z_1, x_j), its width is Δx and height is $\Delta z = h(x,t)$. This cell is bounded above by $\eta(x,t)$, and below by $-d(x)$, its left and right boundaries are $x_{j-\frac{1}{2}}$ and $x_{j+\frac{1}{2}}$, respectively. Every time iteration the cell thickness Δz changes, but its width is constant Δx.

Below are notations for independent variables with indexes

$$h(x_j, t_n) \equiv h_j^n, j = 1,2,...,Nx; \tag{7a}$$

$$q(x_j, t_n) \equiv q_j^n, j = 1,2,...,Nx; \tag{7b}$$

$$u\left(x_{j+\frac{1}{2}}, t_n\right) \equiv u^n_{j+\frac{1}{2}}, j = 0,1,...,Nx; \tag{7c}$$

$$w\left(z_{i+\frac{1}{2}}, x_j, t_n\right) \equiv w^n_{i+\frac{1}{2},j}, i = 0,1 \quad j = 1,2,...,Nx; \tag{7d}$$

$$b\left(x_{j+\frac{1}{2}}\right) \equiv b_{j+\frac{1}{2}}, j = 0,1,...,Nx. \tag{7e}$$

Consistent discretization of (6) is as follows

$$\frac{h_j^{n+1} - h_j^n}{\Delta t} + \frac{(hu)^n_{j+\frac{1}{2}}}{b^n_{j+\frac{1}{2}}}\frac{\left(b^n_{j+\frac{1}{2}} - b^n_{j-\frac{1}{2}}\right)}{\Delta x} + \frac{(hu)^n_{j+\frac{1}{2}} - (hu)^n_{j-\frac{1}{2}}}{\Delta x} = 0, \tag{8a}$$

$$\frac{u^{n+1}_{j+\frac{1}{2}}-u^{n}_{j+\frac{1}{2}}}{\Delta t}+uu_x+g\frac{h^{n+1}_{j+1}-h^{n+1}_{j}}{\Delta x}+\frac{q^{n}_{j+1}-q^{n}_{j}}{\rho\Delta x}+\frac{gnu^{n}_{j+\frac{1}{2}}\left|u^{n}_{j+\frac{1}{2}}\right|}{h^{\frac{4}{3}}_{j}}=0, \tag{8b}$$

$$\frac{w^{n+1}_{\frac{1}{2},j}-w^{n}_{\frac{1}{2},j}}{\Delta t}+\frac{q^{n}_{s}-q^{n}_{j}}{\rho\Delta z}=0, \tag{8c}$$

$$\frac{u^{n+1}_{j+\frac{1}{2}}-u^{n+1}_{j-\frac{1}{2}}}{\Delta x}+\frac{w^{n+1}_{\frac{1}{2},j}-w^{n+1}_{\frac{3}{2},j}}{\Delta z}=0, \tag{8d}$$

where

$$\left(hu\right)^{n}_{j+\frac{1}{2}}=^{*}h^{n}_{j+\frac{1}{2}}u^{n}_{j+\frac{1}{2}}. \tag{9}$$

Variable h^{n}_{j} does not lie in the half grid so that it is denoted as $^{*}h^{n}_{j+\frac{1}{2}}$ and the value is approximated by first-order upwind method, i.e.

$$^{*}h^{n}_{j+\frac{1}{2}}=\begin{cases}h^{n}_{j} & if\ u^{n}_{j+\frac{1}{2}}\geq 0,\\ h^{n}_{j+1} & if\ u^{n}_{j+\frac{1}{2}}<0.\end{cases} \tag{10}$$

Simpler equations can be obtained by adopting the fact that dynamic pressure is zero along the surface qs=0, also vertical velocity is zero along the bottom boundary w3/2=0. The non-linear advection term in (8b) is approximated using the momentum conservative scheme, as described in Stelling and Duinmeijer (2003).

Next, the non-hydrostatic staggered scheme above is solved using the predictor-corrector procedure. First, the predictor step calculates the velocity u and w without the hydrodynamic pressure q. Then, the corrector step updates the predicted value velocity u and w using the hydrodynamic pressure q. Therefore q should be calculated first. So, the computational algorithm of the non-hydrostatic scheme are as follows

1. Compute the water depth hn+1 and the predicted velocity u* using hydrodynamic model

$$h^{n+1}_{j}=h^{n}_{j}-\frac{\Delta t\left(hu\right)^{n}_{j+\frac{1}{2}}}{b^{n}_{j+\frac{1}{2}}\Delta x}\left(b^{n}_{j+\frac{1}{2}}-b^{n}_{j-\frac{1}{2}}\right)-\frac{\Delta t}{\Delta x}\left(\left(hu\right)^{n}_{j+\frac{1}{2}}-\left(hu\right)^{n}_{j-\frac{1}{2}}\right). \tag{11}$$

$$\begin{cases}u^{*}_{j+\frac{1}{2}}=u^{n}_{j+\frac{1}{2}}-\frac{g\Delta t}{\Delta x}\left(h^{n+1}_{j+1}-h^{n+1}_{j}\right)\\ -\Delta t\,uu_x\big|^{n}_{j+\frac{1}{2}}-\frac{g\Delta tnu^{n}_{j+\frac{1}{2}}\left|u^{n}_{j+\frac{1}{2}}\right|}{h^{\frac{4}{3}}_{j}},\end{cases} \tag{12}$$

2. Compute the predicted hydrodynamic pressure q^{*} using formula

$$q^{*}_{j}=\frac{\rho}{\Delta t}\left[\left(u^{*}_{j+\frac{1}{2}}-u^{*}_{j-\frac{1}{2}}\right)h^{n+1}_{j}+w^{*}_{\frac{1}{2},j}\Delta x\right]. \tag{13}$$

3. Compute the hydrodynamic pressure q_{n+1} with successive over relaxation (SOR) iteration method using formula

$$q^{r+1}_{j}=\left(1-\Omega\right)q^{r}_{j}+\frac{\Omega}{a_0}\left[a_1\left(q^{r}_{j+1}+q^{r+1}_{j-1}\right)-q^{*}_{j}\right] \tag{14}$$

Where $a_1=\frac{h^{n+1}_{j}}{\Delta x}$ and $a_0=2\left(\frac{h^{n+1}_{j}}{\Delta x}+\frac{\Delta x}{h^{n+1}_{j}}\right)$. In SOR, starting with $q^{0}_{j}=0$ as the initial guess, we compute q^{r+1}_{j} iteratively for $r=0,1,2,....$ Here we used $\Omega=1.4$. The above iteration is repeated until the solution converged, i.e. $q^{r+1}_{j}-q^{r}_{j}<\varepsilon$ where ε is the tolerance, here taken to be 10^{-5}. The SOR iteration results are q^{n+1}_{j}.

4. Using computed q^{n+1}_{j} to correct the velocities u^{n+1} and w^{n+1} using formula

$$\begin{cases}u^{n+1}_{j+\frac{1}{2}}=u^{*}_{j+\frac{1}{2}}-\frac{\Delta t}{\rho\Delta x}\left(q^{n+1}_{j+1}-q^{n+1}_{j}\right),\\ w^{n+1}_{\frac{1}{2},j}=w^{n}_{\frac{1}{2},j}+\frac{2\Delta t\,q^{n+1}_{j}}{\rho h^{n+1}_{j}}\end{cases} \tag{15}$$

Note that the hydrostatic model consist only two dependent variables $h\left(x,t\right)$ and $u\left(x,t\right)$, and hence its discrete formulation is just $\left(8a,\,8b\right)$ with the dynamic pressure q^{n}_{j} is taken to be zero.

3. VALIDATION OF THE HYDROSTATIC SCHEME

In this section we will conduct several simulations to test the hydrostatic staggered grid scheme. The first and foremost test is, ensuring that our numerical scheme can capture the accurate bore speed. For that purpose we first recall the analytic velocity formula for a bore in a rectangular canal.

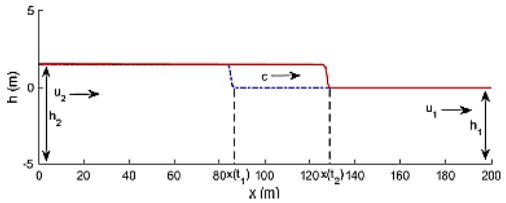

Fig. 3. Sketch and notations of a bore with propagation speed c.

Consider a bore that propagates to the right with velocity c, see Fig. 3. In that figure u_i denotes the horizontal velocity of fluid particles and h_i the water depth, with index $i = 2$ and $i = 1$ denotes the location at front and behind the tidal bore, respectively. The relation between flow properties in front of and behind the tidal bore front can be obtained from mass conservation and momentum balance, which is as follows

$$(u_1 + c)h_1 = (u_2 + c)h_2, \tag{16a}$$

$$\frac{1}{2}gh_1^2 + (u_1 + c)^2 h_1 = \frac{1}{2}gh_2^2 + (u_2 + c)^2 h_2. \tag{16b}$$

where c is the bore velocity. If we eliminate $u_2 + c$ from $(16a)$ and $(16b)$ and after some algebraic manipulation, we obtain a quadratic equation for the ratio $\frac{h_2}{h_1}$. One root is negative, and the other root is positive, which leads to one valid solution

$$\frac{h_2}{h_1} = \frac{1}{2}\sqrt{1 + 8Fr^2} - 1, \tag{17}$$

With

$$Fr = \frac{u_1 + c}{\sqrt{gh_1}}. \tag{18}$$

If we assume $h_2 \geq h_1$, then $Fr^2 \geq \frac{15}{8}$. This is to confirm that a bore will only exist if the flow is super critical.

Further, the bore velocity c can be obtained from (17) by substituting the Froude number formula in the case of $u_1 = 0$ or $Fr = c/\sqrt{gh_1}$. After some manipulation we obtained the bore velocity formula

$$c^2 = \frac{g}{2}\frac{h_2}{h_1}(h_1 + h_2). \tag{19}$$

This bore velocity depends on water depths behind and in front of the tidal bore h_2 and h_1, respectively.

The first three simulations in this section are conducted to test the validity of the hydrostatic scheme in simulating a bore. The first two simulations are for homogeneous canals, whereas the third simulation uses the non-homogeneous canal.

Test case 1: A bore induces by a discontinuous initial surface

The first simulation uses the initial free surface of a piece-wise constant function

$$h(x,0) = \begin{cases} 10, & x < 50 \\ 5, & x > 50 \end{cases}, \quad u(x,0) = 0.$$

Computations were conducted in a computational domain $0 < x < L = 200$, whereas the left and right boundaries are taken to be hard wall boundaries $u(0,t) = 0$, $u(L,t) = 0$. Right after the simulation started, the free surface fell and developed a bore that propagate with a constant speed. Surface profile at time $t_1 = 10$ and $t_2 = 15$ together with the initial surface is plotted on Fig. 4. From the numerical results at time $t = 10$ the bore is located at 142.5, and when $t = 15$ it has moved to 188.7. The numerical bore velocity is obtained from the difference between bore positions divided by the time difference, and we obtained the numerical bore velocity is $c_{num} = 9.24$, to be compared with the analytic bore velocity c_{anal} = 9.35. The Froude number of this simulation is $Fr = >1.34$.

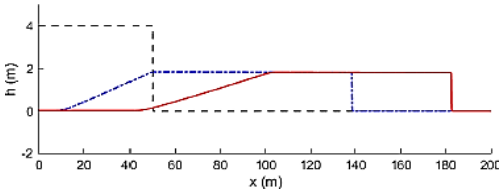

Fig. 4. Snapshots surface profile in test case 1 at subsequent times $t = 0$ s (dashed black line), $t = 10$ s (dashed blue line) and $t = 15$ s (solid red line). The initial discontinuous surface develop into a bore that propagates with constant velocity c_{num}.

Test case 2: A bore induces by left current influx In the second simulation, tidal bore is generated by imposing a left horizontal velocity $u(0,t) = 3$ into the steady water depth $h(x,0) = 7.37$. This left influx gave rise to water height up to $h_2 = 6.53$ and developed a bore. This bore propagates into the domain with constant speed. Simulation results at time $t_1 = 10$ and $t_2 = 15$ are plotted in Fig. 7. By measuring the difference between bore positions within 5 sec time, the numerical bore velocity is 1 obtained, i.e. $c_{num} = 9.34$. This value is to be compare with the analytical bore velocity $c_{anal} = 9.45$. In this simulation we also measure the Froude number, and that is $Fr = >1.35$.

Test case 3: A bore in a non-homogeneous canal In the third simulation, the same setting like the previous simulation is used. The difference is only here we use a non-homogeneous canal. The canal length is 200 m, the width of the upstream part is 20 m and it decreases linearly up to 5 m in the down-

stream part. The same left influx $u(0,t) = 3$ was imposed to the left boundary, which results in an increase of water level. This increase in water level is enforced further by the decrease of canal width. The numerical bore velocity at time t = 15 is cnum = 10.43. In this simulation we also measure that the Froude number is Fr = 1.39.

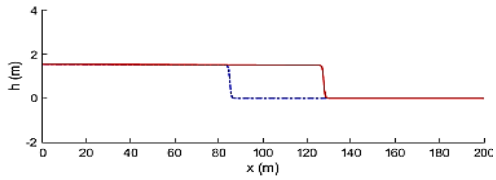

Fig. 5. Snapshots of surface profile in test case 2 plotted at subsequent times $t = 10$ s (dashed blue line) and $t = 15$ s (solid red line). A bore is developed due to left current influx.

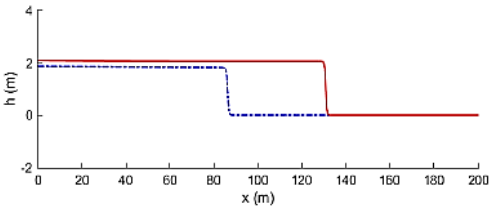

Fig. 6. Snapshots of surface profile in testcase 3 at subsequent times $t = 10$ s (dashed blue line) and $t = 15$ s (solid red line). A bore which is developed due to left current influx, propagates into a narrowing canal.

Table 1 Water height h_1, h_2 and bore positions at two different times $x(t_1)$ and $x(t_2)$ measured in all three test cases, to determine the bore velocity c_{num}, to be compared with the analytical prediction c_{anal}.

Case	h_1	h_2	$x(t_1)$	$x(t_2)$	c_{num}	c_{anal}	Fr
1	5	7.27	142.5	188.7	9.24	9.35	1.34
2	5	7.37	93.4	140.1	9.34	9.45	1.35
3	5	8.33	95.6	145.8	10.43		1.39

Results of the three simulations above are resumed in Tabel 1. All simulations are supercritical with Froude number 1.34, 1.35, and 1.39 respectively. It is shown in all cases above, that our numerical simulation can produce a bore front that propagate with velocity c_{num}, that are in good agreement with the analytical bore velocity c_{anal}.

4. NUMERICAL SIMULATION OF THE NON-HYDROSTATIC MODEL

In this section the non-hydrostatic scheme will be used. By performing simulation we will show the occurrence of tidal bore at Kampar river as a result of an interaction between incoming tidal flows with the river current. By using the non-hydrostatic scheme we show the development of undulations that follow the tidal bore.

4.1 A Bore with Undulation

In this section, we adopt the second test case setting but now using but now using the non-hydrostatic scheme. We observe the same tidal bore propagate with the same speed, but now it is accompanied by undulations. The numerical results at time $t = 10$ the bore is located at 73.5, and when t = 15, it has moved to 122. And just like the previous, we obtained the bore propagation velocity $c_{num} = 8.92\ m/sec$, which is to be compared with the analytical bore velocity $c_{anal} = 9.04\ m/sec$. In this simulation we also measure the Froude number, which is $Fr = 1.29$, see Fig. 7.

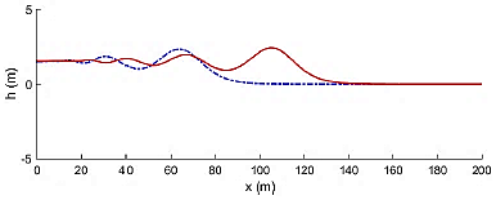

Fig. 7. Snapshots of surface profile in test case 2 at subsequent times $t = 10$ s (dashed blue line) and $t = 15$ s (solid red line). Using the non-hydrostatic scheme, the propagating bore is now followed with an undulation.

4.2 Numerical Simulation of Tidal Bono

In this section, our numerical scheme is used to simulate the appearance of Bono wave due to tidal flow. We use Kampar River topography depicted in Fig. 14, as in Rahmawan, et. al. (2016). In that figure the computational domain is indicated as the red solid line. This line also represent the river stream.

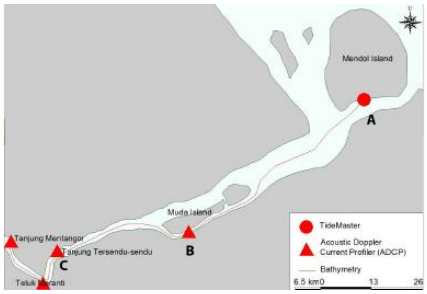

Fig. 8. Kampar River with three sites of field measurements; site A: semi-diurnal tides, site B and C: Bono waves. The black line indicates the computational domain.

The Global Mapper 17 application was used to construct Kampar River topography, by first recorded the river depth along this red line. Then, the river widths were obtained of direct measurement from Google Earth photo. Finally, the constructed three-dimensional bathymetry of Kampar River is depicted in Fig. 9.

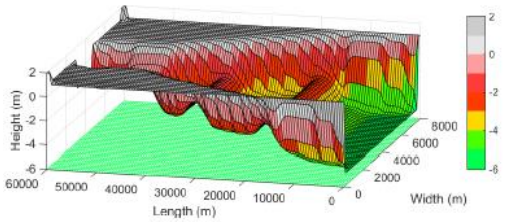

Fig. 9. Model bathymetry of Kampar River.

Bono waves in Kampar River were generated by tidal stream entering the river mouth and propagating upstream. This tidal stream is a semi diurnal tides with period 12 hour 25 minutes (Yulistiyanto, 2009). The researchers team from RICRV conducted field measurement at several places along the Kampar River. Stream flow was measured using Acoustic Doppler Current Profiler, whereas tidal wave height was measured using Tide Master. Figure 10 displays a tidal wave height measured at the point A for the period April - May 2016, as recorded previously in Rahmawan et.al. (2016). Tidal wave height as shown in Fig. 10 (inset) was used as a boundary condition to the initial still water level $h(x,0) = 0$, $u(x,0) = 0$, $w(x,0) = 0$. The height of this tidal wave ranges from 1-5 m at night and 1.5-4 m in the afternoon. Parameters used in this computation are $g = 9.8\, m/s^2$, $\rho = 1024\, kg/m^3$, and the Manning friction coefficient is taken to be n=0.001, with step size $\Delta x = 10\, m$, $\Delta t = 0.5\, s$. This tidal flow induces a Bono wave that travel further into the domain. At the point C, the wave height h wasrecorded, and the result is compared with measurement.

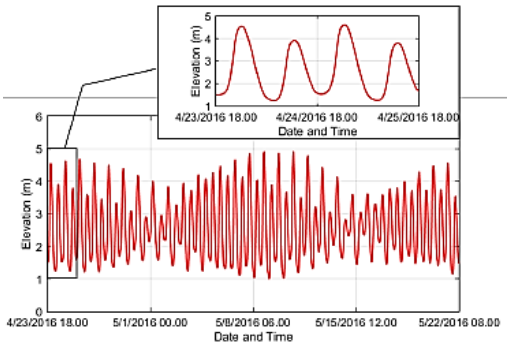

Fig. 10. Water height of a semi diurnal tides with period 12 hour 25 minutes, as measured at point A. High tide ranges between 1−5 meters, and low tide ranges between 1.5 − 4 meters. (Inset) Tidal wave data used in our simulation.

As shown in Fig. 11 that evening tides produce higher Bono waves, which is about 4 m, whereas daytime the day the height of Bono wave is about 3.4 m. Figure 11 shows that when compared with the measurement, our simulation can predict the Bono wave quite well.

Further comparison is conducted for horizontal velocity u which is recorded at point C, and the result is compared with measurement. The result as depicted in Fig. 12 shows that our simulation is much higher than measurement. The differences are quite striking between the current measurement and simulation results can be caused by the limitations of measurement versus numerical models. River currents were measured using Acoustic Doppler Current Profiler which are located near the banks of the river, while our simulation uses a model that assumes homogeneity in the direction of the river cross section. Moreover, for efficiency reasons our model applies hydrodynamic pressure approximation using one layer only, which is also an approximation.

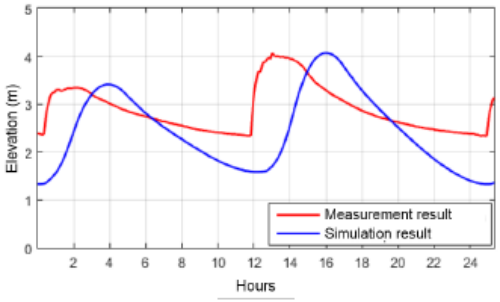

Fig. 11. Plots of water height at point C, obtained from simulation and measurement.

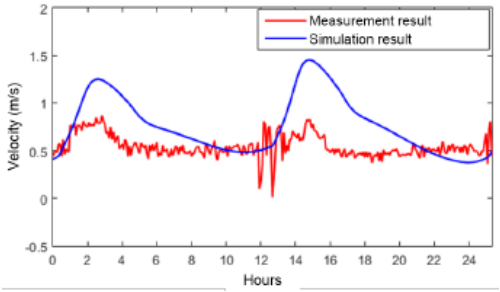

Fig. 12. Plots of horizontal velocities u at point C, obtained from simulation and measurement.

4.3 The Lost Bore Scenario

Here we conduct a simulation which is similar with the test case 3 in Section 3 but instead of narrowing canal, we use a widening canal with length 200 m, and width 5 m (upstream) and 20 m (downstream). The left boundary $u(0,t) = 2\, m/s$ is imposed into a fixed water depth $h(x,0) = 5\, m$. As expected, this left influx induces a tidal wave that propagate downstream. But as shown in Fig. 13, the amplitude of this tidal wave decreases significantly as time progresses.

The second scenario is enforcing a subcritical flow simulation. This is done by giving somewhat low left influx $u(0,t) = 0.5$ into somewhat large water depth $h(x,0) = 10$ in a rectangular canal. Under this setting, the left influx did not produce a noticeable bore wave, and tidal bore does not occur.

In this simulation $h_2 \approx h_1 = 10$, and the Froude number computed from (18) is $Fr = 1.04$, which is less than 15/8, and hence, as predicted from (17) the bore wave does not appear.

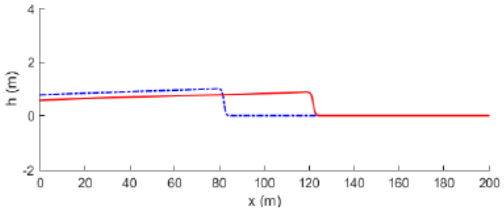

Fig. 13. Surface profile in the simulation of lost Bono scenario 1. It is shown that the bore height decreases as it propagates further downstream.

5. CONCLUSIONS

The staggered grid scheme of the Saint Venant equations was shown to be suitable and accurate for simulating various tidal bore scenarios, subsequently by incorporating the hydrodynamic pressure, an undular bore that follows the shock front emanates. By adopting tidal current data obtained from measurement, the formation of tidal bore Bono was simulated. The comparison between the numerical surface and the surface measurement at Tanjung Tersendu-sendu has shown a good agreement. Through a good understanding of the physical mechanisms of a tidal bore, we hope that the tidal bore Bono in Kampar River can be maintained properly.

ACKNOWLEDGMENT

The authors acknowledge the field data provided by the Research Institute of Coastal Resources and Vulnerability (RICRV) Padang - West Sumatera. Pudjaprasetya would like to thank Institut Teknologi Bandung for the Financial support from Riset KK with contract 107a/I1.C01/PL/2017.

REFERENCES

Aldrighetti, E. (2007). *Computational hydraulic techniques for the Saint Venant Equations in arbitrarily shaped geometry*. Ph. D. thesis, Universita` Degli Studi di Trento, Trento, Italy.

Bayu, A. C., S. R. Pudjaprasetya and I. Magdalena (2017). Three-layer nonhydrostatic staggered scheme for free surface flow. *East Asian Journal on Applied Mathematics* 7(4), 643˚ 657.

Chanson, H. (2009). Environmental, ecological, and cultural impacts of tidal bores, benaks, bonos and burros. In P. I. R. G. L. P. F. M. S. G. P. S. P. A. Lopez-Jimenez, V. S. Fuertes-Miquel (Ed.), Proceedings of the International Workshop on Environmental Hydraulics IWEH09, Theoretical, Experimental and Computational Solutions, Valencia, Spain, pp. 1˚20. International Workshop on Environmental Hydraulics.

Kim, D. H. and P. J. Lynett (2011). Dispersive and nonhydrostatic pressure effects at the front of surge. *Journal of Hydraulic Engineering* 137, 754˚765.

Rahmawan, G. A., U. J. Wisha, S. Husrin and Ilham (2016). Bathymetry and tidal analysis for Kampar Big River Estuary: Generate of Tidal Wave Propagation Undular Bore Bono, Geomatika 22(2), 57-64.

Stelling, G. S. and S. P. A. Duinmeijer (2003). A staggered conservative scheme for every froude number in rapidly varied shallow water flows. *International Journal for Numerical Methods in Fluids* 43(12), 1329˚1354.

Vo Thi, N. T. (2008). *One dimensional saintvenant system. analysis of pdes*. Master sthesis, Universite d Orleans, Orleans, France.

Yulistiyanto, B. (2009). The phenomenon of bono rising wave in kampar river estuary. *Dinamika Teknik Sipil* 9(1), 19˚26.